AIAA AVIATION Forum
13-17 June 2016, Washington, D.C.
8th AIAA Flow Control Conference

On the effect of discrete roughness on the growth of crossflow instability in very low turbulence environment

Marco Placidi* , Evelien van Bokhorst†
and Chris J. Atkin‡
City University London, London, EC1V 0HB, UK

Wind tunnel experiments were conducted in a low-turbulence environment ($Tu < 0.006\%$) on the stability of 3D boundary layers. The effect of two different distributions of discrete roughness elements (DREs) on crossflow vortices disturbances and their growth was evaluated. As previously reported, DREs are found to be an effective tool in modulating the behaviour of crossflow modes. However, the effect of $24\mu m$ DREs was found to be weaker than previously thought, possibly due to the low level of environmental disturbances herewith. Preliminary results suggest that together with the height of the DREs and their spanwise spacing, their physical distribution across the surface also intimately affects the stability of 3D boundary layers. Finally, crossflow vortices are tracked along the chord of the model and their merging is captured. This phenomena is accompanied by a change in the critical wavelength of the dominant mode.

Nomenclature

c	Model chord
h	Roughness height
D	Roughness diamater
λ	Roughness spanwise spacing
(x, y, z)	Streamwise, wall-normal and spanwise directions
U	Mean streamwise velocity component
U_e	Edge velocity
u'	Fluctuating streamwise velocity component
C_p	Pressure coefficient
A	Amplitude of crossflow mode
A_0	Amplitude of crossflow mode at the first measurement station
x_T	Laminar-turbulent transition location

I. Introduction and background

A thorough understanding of the mechanisms behind the transition from laminar to turbulent flow is of vital importance for the aerospace industry given the importance of minimising both fuel consumption and pollutant emissions. The benefits of hybrid laminar flow flight, in fact, are estimated to reach goals up to 1.6% net reduction in the total aircraft drag (Atkin, 2004). Shedding light onto the transition process is also fundamental for the accurate prediction of aerodynamic forces (i.e. lift and drag) and heating requirements (Reed and Saric, 1996). Rare flight tests (Carpenter et al., 2009; Saric, 2008b) have recorded extremely low level of freestream turbulence in flight condition (i.e. $0.05\% - 0.06\%U_\infty$). However, most of the modern

*Research Fellow, SMCSE, Northampton Square EC1V 0HB;
†Ph.D candidate, SMCSE, Northampton Square EC1V 0HB;
‡Professor of Aeronautical Engineering, SMCSE, Northampton Square EC1V 0HB

low-turbulence wind tunnels are not low-turbulence in a significant frequency range (Kachanov, 2000). This together with our poor understanding of the transition process, has lead to the fact that our predictions of the transition onset are often unreliable (Saric, 2008a; Saric et al., 2002). This is also aggravated by the variety of factors that can affect the transition process: freestream turbulence (Choudhari, 1994), surface roughness (Saric et al., 2002), acoustic field (Shapiro, 1977), amongst many others. It is well-known that there are different type of instabilities depending on the geometric characteristics of the problem in investigation and consequently different transition paths (Morkovin, 1969). Comprehensive reviews on typical transition scenarios can be found in Kachanov (1994); Morkovin (1969); Reed and Saric (1996); Reshotko (1976); Saric et al. (2002); Tani (1969).

Since Gray (1952), it is well established that the stability of 3D boundary layers is dominated by crossflow vortices (CFVs). Excellent reviews on this topic are contained in (Bippes, 1999; Dagenhart, 1992; Reed and Saric, 1989; Saric and Reed, 2003; Saric et al., 2003). Briefly, these co-rotating CFVs (almost aligned with the inviscid streamline) are generated due to the combined effect of sweep and favourable pressure gradient and they are believed to be particularly sensitive to the morphology of the surface they develop above. Bippes and coworkers carried out numerous experiments on the stability of 3D boundary layers (see Bippes (1999) for a full review). Particularly relevant herein is the work of Deyhle and Bippes (1996), who carried out a series of experiments with varying the disturbance environment and revealed that, in the presence of crossflow instability, the boundary layer is extremely sensitive to surface roughness. They also suggested that only at values of turbulence intensities $Tu > 0.2\%$, the travelling waves become dominant, although a slight dependence on the surface roughness height was also suggested. Given the latter, a great deal of attention has been given in recent years to flow-control strategies based on discrete micron-sized circular roughness elements (DREs). Radeztsky (1994) firstly showcased the potential of these technology by placing an array of spanwise periodic DREs in correspondence of few percent chord (i.e. in proximity of the neutral stability point (NSP) according with linear stability theory). Reibert (1996) carried out experiments on the effect of DREs on the non-linear development and growth of CFVs. This work focused on the effect of roughness spacing, roughness height and Reynolds number. The transition location was found to be largely unaffected by the roughness height (in the range $6 - 48\ \mu m$), however, a two-stage saturation was observed when the roughness height became significant. This is generally followed by a relaxation phase, which counteracts the two-stage growth. On the contrary, the spacing of the roughness was reported to plays a more important role in transition onset. White and Saric (2005) shed light into the breakdown mechanism of crossflow-dominated 3D boundary layers. They reported a rapidly growing high-frequency secondary instability characterising the stationary crossflow vortices, which was found to grow much more rapidly than the low-frequency mode associated with travelling crossflow wave. This secondary instability, possibly in combination with the low-frequency fluctuations, was pinpointed as responsible for the breakdown. More recently, Hunt (2011) used the same DREs concept to investigate the region of linear stability in a stationary crossflow dominated transition at low turbulence intensities (i.e. $Tu < 0.02\%$). It was found that, in this linear region, the disturbance amplitude varies almost linearly with roughness height. To conclude, from the work of Saric and coworkers, one clear potential benefit of DREs is that they can be employed to excite subcritical CF wavelengths, which have the potential to prevent the most unstable mode (i.e. the critical wavelength mode) from growing, hence delaying the turbulent onset. Appropriately spanwise spaced roughness have been demonstrated to be capable of delivering extended laminar flow both in laboratory experiments (Hunt, 2011) and flight tests (Crawford et al., 2015; Tufts et al., 2014). A recent experiment also examined the effect of DREs in a moderate-level disturbance facility (Saeed et al., 2014). Despite the level of environmental disturbance, they confirmed that the flow was dominated by stationary CFVs. An increased roughness height was found to advance transition, introducing mean-flow deformation in the velocity profiles and high-frequency spectral content in the fluctuations. Last but not least, many numerical simulations have also devoted effort to predict the stability of roughness induced crossflow (Bertolotti, 2000; Carpenter et al., 2010; Mughal and Ashworth, 2013; Tempelmann et al., 2012, amongst others).

All these previous studies on DREs, however, have focused on highly idealised roughness configurations arranged on a single array. This type of morphology is not representative of the real wing-skin roughness (e.g. due to wear and icing) and its applicability as a means of flow control on commercial aircraft is yet to be demonstrated. Therefore, the scope of this work is to pave the way for more realistic roughness morphologies by combining single arrays of DREs into more complicated three-dimensional patterns. This will allow us not only to test our theoretical understanding of the transition mechanisms but also to shed some light on how these mechanisms relate and scale with the geometry of the problem in examination. This work also

aims at providing benchmark data to support numerical prediction methods.

II. Methodology and details

The structure of this section is as follows: §A introduces the experimental facility, while §B describes the model in use; then, the instrumentation for the data handling are described in §C. §D deals with the surface roughness specifications. Finally, a discussion on the hot-wire scans and the determination of the transition location are discussed in §E and §F, respectively.

A. Experimental facility

Experiments were carried out in the closed-loop Gaster low-turbulence wind tunnel at City University London, which is part of UK's National Wind Tunnel Facility (NWTF). The turbulence intensity measured in the empty tunnel was less than $0.006\%U_\infty$ within the frequency range $4Hz-4kHz$ at a freestream velocity of 16 ms^{-1} (i.e. the one used throughout the course of this study). These levels of turbulence are representative of flight conditions (Carpenter et al., 2009; Saric, 2008b). The tunnel test section measures 3 $ft \times 3$ $ft \times 6$ ft. The velocity in the working section was kept to 16 ± 0.2 ms^{-1} throughout the tests. The wind tunnel is equipped with a 3-axis traverse system, which has a minimum step size of 10, 6.25 and 7.5 μm for the x, y and z directions respectively. Here, x, y and z are the streamwise, wall-normal and spanwise directions. The mean and fluctuating streamwise velocities are identified by U and u'. The term fluctuating is hereafter assumed to refer to the band-pass filtered AC component of the hot-wire signal, often presented as its root mean square (rms).

B. Experimental setup

As briefly discussed in § I, the development of CFVs relies on the combined effect of sweep and pressure gradient. A 45 degree swept flat plate under the effect of an equally swept displacement body, which creates the optimal favourable pressure gradient ($dp/dx < 0$) is used herein. To guarantee a symmetric flow and to prevent the stagnation point from meandering across the different configurations (and hence modifying the circulation on the plate) two identical displacement bodies are placed both above and below the flat plate, as shown in figure 1.

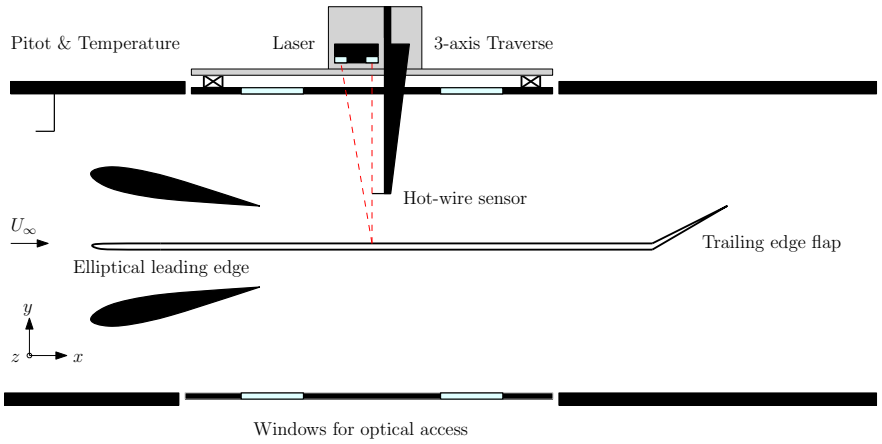

Figure 1. Schematic representation of the experimental setup. Top view of the test section illustrating its different components.

This setup has the advantages of offering a reduced complexity in the traverse movements when acquiring the data, the possibility of arbitrarily modifying the pressure gradient in accordance to the experimental requirements and it favours the generation of *quasi*-2D flow hypothesis, as further discussed in Bippes (1999). In order to design the displacement bodies (DBs) geometry, a Hess-Smith panel code was developed and a multi-objective optimisation was carried out. Details of the design process are here omitted for the sake

of brevity but these are contained in van Bokhorst et al. (2015). The final design choice was evaluated by comparing the obtained pressure gradient with previous studies on CFVs (Bippes et al., 1991; Hunt, 2011; Reibert, 1996). Once the geometry of the model was fully defined, a combination of a numerical boundary layer solver and linear stability analysis were used to verify that the chosen setup would promote the growth of CF instabilities, whilst dampen the T-S waves (see van Bokhorst et al. (2016) for further details). The outcome of this preliminary analysis motivated the use of a type *lwk80100* wing (Mangalam and Pfenninger, 1984) with chord length, $C_{DB} = 0.4\ m$, mounted at an angle of attack of 11 degrees and at a wall-normal distance of 0.1 m from the plate. This configuration is shown in figure 1. Once the model was mounted in the test section, the freestream turbulence intensity was monitored. It was registered to be below 0.012% within the frequency range $2Hz - 10kHz$ (used throughout the data acquisition) at a freestream velocity of nominally 16 m/s. This is well below the limit of $0.1 - 0.2\%$ where travelling instabilities are believed to dominate the transition process (Crouch et al., 2015; Deyhle and Bippes, 1996; Radeztsky et al., 1999).

C. Instrumentation and data acquisition

Constant temperature hot wire anemometry (CTA) is chosen as main experimental technique since it allows for measurements with both high spatial and temporal resolutions without the requirements for seeding particles, which are believed to have a detrimental effect on low-turbulence wind tunnel performance, as they contaminate the screens. The flow velocity and fluctuations are measured by traversing a tungsten *Dantec* hot-wire sensor (with effective sensing length $l \approx 1mm$ and diameter $d \approx 5\mu m$) in the flow. This sensing length satisfies Ligrani and Bradshaw's (1987) criterion to avoid probe end effects. The analog signals (i.e. pressure transducer, hot wire sensor, temperature sensor, etc.) are digitised using an *NI PXI6143* card in combination with a *DAQ-BNC2021* data acquisition module. These are coordinated via a PXI Chassis (*NI PXI 1033*), which is operated by an in-house data acquisition system in *LabVIEW* software. The sample duration is 5 s for all the measurements and the sample frequency is fixed at 20 kHz. Low-pass and high-pass filters are controlled via a filter (*PDS Instruments ltd. 3362*) and set to 10 kHz and 2 Hz, respectively. The volt to velocity conversion is obtained via King's law fit and temperature correction is applied to compensate for any change in the temperature during a run, as highlighted in Bruun (1995). To minimise the calibration error, the probes are calibrated in-situ in the velocity range $0.5\ m/s \leq U \leq 20\ m/s$ against a Pitot-static tube connected to a *Furness* (FCO560) manometer. The latter has a resolution of 0.025% its full scale range, herein $\pm 15\ Pa$. The static pressure on the model is also monitored via static pressure ports (outer diameter of 0.5 mm) embedded in the surface and connected to the Furness pressure transducer. Three rows of pressure ports are used to ensure that the flow is two-dimensional in the measurement region and that the model is well positioned in the test section.

D. Surface roughness

Roughness in the form of DREs is typically used to control CFVs. Circular DREs are placed parallel to the leading edge (i.e. at a fixed x/c) in close proximity of the neutral stability point ($x/c = 4\%$) as is in this location that they are believed to be most efficient in generating maximum growth (Radeztsky et al., 1999).

Table 1. Relevant experimental parameters for the DREs.

Case ID	Position (x/c)	Roughness type	$h(\mu m)$	No. arrays	Measurement (x/c)
Natural	—	—	—	—	35, 40, 45, 48, 50 %
L11_H24_1R	4%	circular DREs	24	1	35, 40, 45, 48, 50 %
L11_H24_2R	$4 - 5\%$	circular DREs	24	2	35, 40, 45, 48, 50 %

The main critical parameters that defined these discrete roughness elements are the height, diameter and spanwise spacing in between the roughness elements; these are denoted with h, D and λ respectively. The spanwise spacing between the DREs (i.e. the wavelength) is herein determined via a combination of a boundary layer solver and linear stability analysis to be $\lambda = 11.5\ mm$. The diameter of the DREs was chosen to be $D = 3\ mm$, as previous studies (Radeztsky et al., 1999) have shown that to obtain significant effects this should be so that $D/\lambda = 0.3 - 0.4$. The height of the DREs is perhaps the most important parameter as it determines the magnitude of the disturbances on the flow. The roughness Reynolds number,

$Re_h = U_h h/\nu$, where U_h is the correspondent Blasius (1908) velocity at the roughness height and ν is the dynamic viscosity, should not exceed a critical number (approximately $Re_{cr} = 300 - 600$) to prevent 'bypass transition' (Morkovin, 1969). As the aim of the current set of experiments is to study the development and growth of the crossflow instability, it is required to keep the roughness conservatively below the critical value. We opted for the thinnest roughness elements commercially available. Appliqué roughness elements of nominally 6 μm were chosen, as in previous studies (Hunt, 2011; Saeed et al., 2014, amongst others).

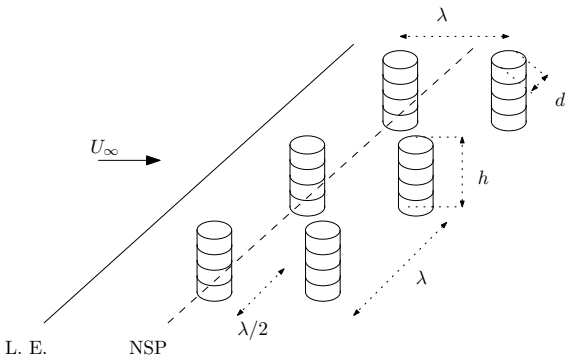

Figure 2. Schematic representation of the DREs setup for L11_H24_2R case.

These elements are printed on a dry-ink transfer sheet and are supplied by *Redd Europe Ltd*$^{\text{TM}}$. Three different configurations are the object of the current investigation, as summarised in table 1. The case ID Natural identifies the benchmark case without artificial roughness, L11_H24_1R case represents the configuration where a single row of cylindrical DREs with spanwise spacing of $\lambda = 11.5$ mm and heigh of $h = 24$ μm is applied in correspondence with the neutral stability point. It is important to note that this height corresponds to a roughness Reynolds number conservatively subcritical. Finally in the L11_H24_2R case, a second identical row of DREs is placed at $\approx 5\%$ chord (i.e. one λ downstream) and staggered by 50%, compared to the previous row of roughness, as shown in figure 2. This configuration is considered based on Reibert (1996)'s finding. It was shown that roughness elements spaced at a spanwise spacing λ only excite disturbances characterised by λ/n wavelengths, while do not effect modes with wavelengths greater than λ. Therefore, given our DREs disposition, this configuration should excite the same modes as the L11_H24_1R case, when neglecting the inclination angle of the inviscid streamline.

E. Hot-wire traverses

The measurements discussed herein are acquired in the coordinate system shown in figure 3. Two types of hot-wire traverses (x)-, and (y-z)- scans were acquired to gain different information. The (x)-scans are used to detect the transition location (as in § F), while the rest of the analysis is carried out on the detailed boundary layer profiles (i.e. (y-z)-scans). The latter are obtained over a ≈ 50 mm long fetch, with a spanwise spacing of 1 mm and 40 points within the wall-normal direction. These spacing should provide enough spatial resolution to resolve the CFVs (Saric, 2008a). Ten different (x)- traverses are instead acquired to detect the transition location. These span the entire (y-z) domain and are acquired with a streamwise spacing of 5 mm, which leads to a ± 5 mm uncertainty on the onset of laminar-turbulent transition. The traverse could not access the region under the displacement body ($x/c < 30\%$) due to the limited space and the necessity of keeping the sensor fairly close to the traverse sting to limit the probe vibration. In addition, data could not be acquired downstream of $x/c = 60\%$ due to the limited range of the traverse (within the tunnel support structure). Given the plate surface imperfections and the uncertainty in the relative position of the traverse system in plate coordinates, simply traversing the hot-wire in the z-direction would result in a significant drift in the mean velocity (i.e. different y/δ across the span). This is a common problem in crossflow studies (Eppink, 2014; Hunt, 2011; Reibert, 1996, amongst others). Therefore a *Micro-Epsilon* (ILD2300) triangulation laser system was embedded in the traverse stand and used to gain the relative distance in between the wall and the hot-wire sensor, as shown in figure 1. The resolution of the laser displacement is below 10 μm. This allows the distance of the hot-wire sensor to the wall to be corrected at each measurement

location, guaranteeing hot-wire recordings at fixed wall-normal locations. Even employing the laser sensor, the wall location still needs to be corrected at each spanwise location by extrapolating the profile at zero velocity. This procedure ignores the slight curvature of the boundary layer due to the pressure gradient by applying a linear fit to the near wall region. This method has been successfully adopted by Dagenhart (1992), Radeztsky et al. (1999) and more recently by Hunt (2011). Once the wall location is determined, each profile is shifted to match the new findings before estimating the stationary CFVs amplitudes. It has been reported that, without this procedure, error up to 40% can effect the crossflow amplitudes (Eppink and Wlezien, 2011). Shifting the velocity profiles, however, results in different wall-normal locations for each spanwise location. Therefore, for the ease of dealing with the data, the velocity field is interpolated onto a new grid, which is constant throughout the measurements domain. This is a common procedure in the literature (Hunt, 2011).

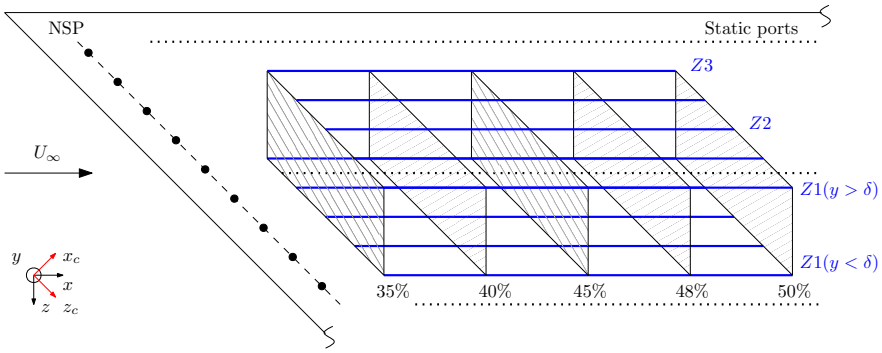

Figure 3. Schematic representation of the test matrix for the $(y-z)$-scans (in black) and the (x)-scans (in blue). Dashed and dotted lines represent the neutral stability point (NSP) and the location of the static pressure ports. DREs are represented by •. Dimensions are not in scale to enhance readability.

F. Transition location determination

Many experimental observations of laminar breakdown in the presence of roughness (Eppink, 2014; Hunt, 2011; Saeed et al., 2014; White and Saric, 2005) have gathered that the onset of turbulence is characterised by the development of a series of spikes in the time series of the hot-wire signal (in according to a 'K-type' breakdown).

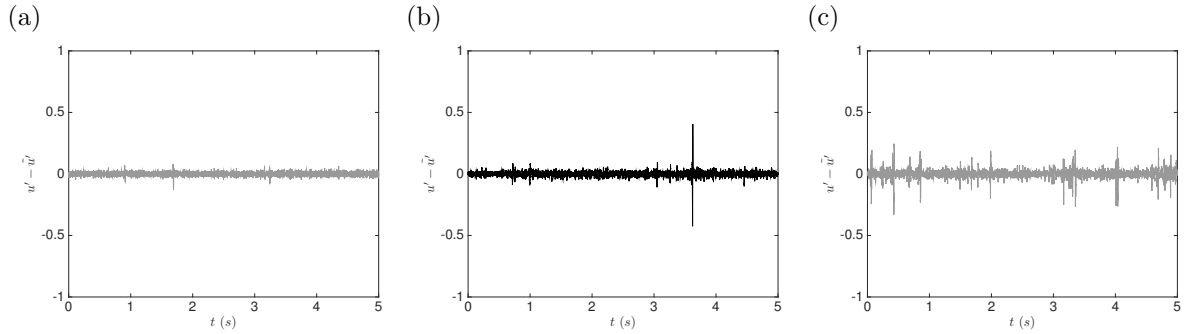

Figure 4. (a) Typical conditioned hot-wire signal before transition onset, (b) conditioned signal at the identified transition location, (c) typical conditioned hot-wire signal past the transition onset.

In this work we attempt to gain a rough indication of the transition location by monitoring the hot-wire signal whilst the probe is traversed downstream at a fixed wall-normal location ($y = 1\ mm < \delta$), as proposed by Wang and Gaster (2005). The detection of these spikes relies on a procedure which involves subtracting a locally smoothen signal (via Gaussian filter) from the original AC band-passed filtered signal. A threshold on the resulting signal ($u' - \tilde{u}' > 0.1$) is then applied to localise the spikes which mark the onset of turbulence. Although the authors are aware of the subjectivity of this threshold choice, given that the same criterion is adopted in all cases contained in this study, it is believed that general trends of the effect of different disturbances on the transition location can be efficiently captured following this approach. An

example of this procedure is illustrated in figure 4. The conditioned signal at the detected transition location is shown in figure 4(b), while typical laminar and turbulent conditioned signal are shown in figure 4(a)&(c), respectively. It is clear to see that the laminar signal (in (a)) appears smooth, the signal in correspondence of the transition detection (in (b)) is characterised by at least one strong spike, while the turbulent signal (in (c)) is much more populated by spikes compared to the previous one.

III. Results and discussion

Before some results are presented and discussed, the validation of our numerical design is briefly considered in § A. Next, a discussion upon mean and fluctuating velocity fields is the object of § B and § C respectively. The evolution of the CFVs is then considered in § D, before § E sheds light into a spatial spectral analysis. Finally, the effect of the DREs on the transition onset location is discussed in § F.

A. Preliminary validation

Given that object of this paper is the first experiment on the stability of 3D boundary layers in the facility described in § II at City University London, great care has been put to ensure that the facility was behaving as expected and that our numerical design was as accurate as possible. In particular, once the flat plate was installed and secured in the test section (prior the installation of the DB), velocity profiles at different x/c and z locations are acquired and compared to the theoretical Blasius's (1908) solution for zero pressure gradient. These results although omitted herein, showed a very close agreement between the theoretical solution and the experimental data. Following these preliminary tests, the pressure coefficient, C_p, was measured and compared with numerical prediction and previous studies. This is omitted here but the reader is referred to figure 9 in van Bokhorst et al. (2016). It is shown that the measured pressure coefficient, C_p, compares well with our numerical predictions. Furthermore, its gradient from ($x/c \approx 0.2$) is similar to previous studies (Bippes, 1999; Hunt, 2011), which indicate the viability of the current setup for the aims of this work.

B. Mean flow fields

It is believed that, for low-turbulence environments (flight conditions $Tu << 0.15\%$ as from (Crouch et al., 2015)), the transition process should be dominated by roughness-induced stationary crossflow instabilities (Radeztsky et al., 1999). On the other hand, travelling waves are considered to be triggered by environmental conditions (Malik et al., 1994). Following these beliefs, given the characteristics of the facility used herein (see § II), we first dedicate our attention to the role of stationary CFVs and therefore to the mean velocity fields. To highlight the main features of the flow in examination, the mean velocity fields at ($x/c = 35\%$) are presented in figure 5. The Natural case, the single row of DREs (i.e. L11_H24_1R) and the two staggered rows of DREs (i.e. L11_H24_2R) are shown in (a), (b) and (c), respectively. For all cases, the boundary layer thickness is reasonably small (i.e. below 3 mm) and the flow is well within the laminar regime, as shown by the correspondent mean velocity profiles in figure 5(d) to (f) (black solid lines), which present Blasius (1908) behaviour. This is in line with previous studies.

For the Natural case (figure 5(a)), the mean flow is shown to be very slightly distorted due to the presence of the CFVs. This influence is, however, much clearer when one looks at the cases where DREs are present (in figure 5(b)&(c)). In particular, to help visualising this feature, red dashed lines are added in figure 5(c) in correspondence of this mean flow modulation. These regions happen to correspond to the spanwise spacing of the DREs and highlight the critical wavelength, $\lambda = 11.5\ mm$, as from LSA. These findings compare well with previous work on DREs, although the mean flow modulation is weaker than previously reported (e.g Hunt (2011)). This could be due to the lower environmental disturbances characterising the current work or to the weaker pressure gradient or, most likely, to a combination of the above. A great deal of effort was dedicated to accurately sealing the wind tunnel test section used herewith. We realised that very small leakages could affect the results of our measurements. Once we eliminated those permanently, we registered a decrease up to one order of magnitude in the freestream turbulence intensity (with the model in situ). Additionally, the DREs resulted less effective and, as expected, the transition front moved backward ($\approx 5\%$ chord). Also shown in figure 5(d) to (f) are around 50 boundary layer profiles (grey lines) at the different spanwise locations but fixed chord; their mean being the black solid line. The rollover, characteristic of nonlinear distortion (Hunt and Saric, 2011) is still not present in these contour plots at $x/c = 35\%$.

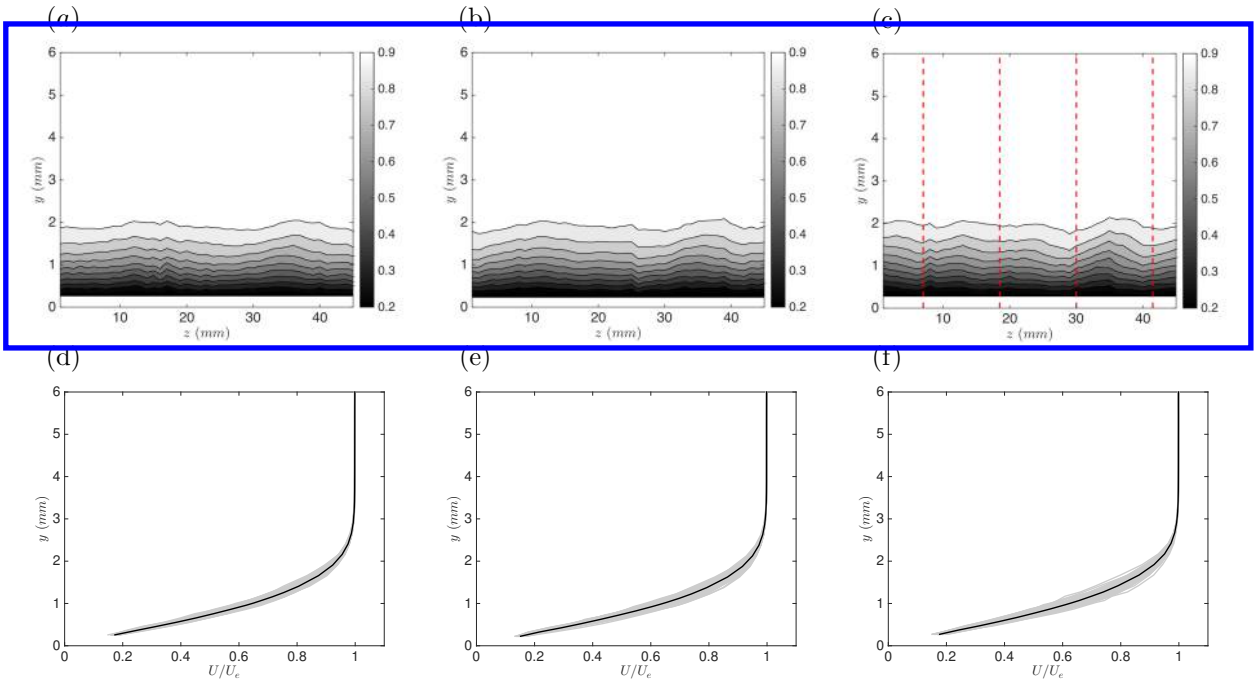

Figure 5. (top) Contour plots of non-dimensional mean velocity profiles , U/U_e, at $x/c = 35\%$ for (a) Natural, (b) L11_H24_1R and (c) L11_H24_2R cases. (bottom) Respective 2D spanwise velocity profiles (grey) and spanwise mean (black).

C. Fluctuating flow fields

To further investigate the flow features, fluctuating velocity fields are presented next. These correspond to the AC band-passed filtered signal at the same locations shown in figure 5. These contour plots are shown in figure 6. The same order is followed, where from (a) to (c) the surface roughness is increased. For all cases, perturbations of streamwise velocity populate the boundary layers, where coherent regions of high-momentum appear to be centred at approximately $y = 1\ mm$. These features have been extensively reported to be the imprint of CFVs (Hunt, 2011; Reibert, 1996; White and Saric, 2005, amongst others).

It is interesting to note that, for the natural cases (figure 6(a)) the spanwise spacing of these vortex cores seem to match theoretical predictions, as it is estimated to be of approximately $\lambda = 10\ mm$. Five vortices are visible across the 50 mm span. Similar conclusions can be drawn by looking at L11_H24_1R case in (b). It should be clear, however, that the strength of these vortices is higher compared to the natural case, as the contour level is kept constant. When the L11_H24_2R case is considered (figure 6(c)), not only the vortices resulted significantly strengthen but also their number seem to have increased. Eight vortices are visible in the same scanned portion of the flow. This could also be an evidence of the early nonlinear interaction between stationary and travelling waves as in Malik et al. (1994). However, this aspect should be further investigated. As for the mean velocity, the variability of the fluctuating fields is also quantified in figure 6(d) to (f) by investigating the quantity $(u' - \overline{u'})/U_e$. What is visually clear from figure 6(a) to (c), is also quantitatively true; by increasing the DREs on the plate surfaces, the strength and variability of the disturbances within the boundary layer tent to increase. From this very preliminary assessment, it can be inferred that, when DREs are employed, they act upon the CF disturbances, imposing order and amplifying them. This is so far in agreement with previous studies that showcase the capacity of these discrete roughness of interacting with the natural structure of the flow. Before we shift our focus to the development of the CFVs, it is useful to trying to establish a link in between the mean fields presented in figure 5 and the fluctuating field in figure 6. Zoomed view of both fields for the L11_H24_2R case are reported side to side in figure 7(a)&(b). Both fields are divided in three complete slices of size λ by dashed red lines. It is easy to visualise in this format, that the mean flow modulation is due to the presence of the CFVs. In particular a

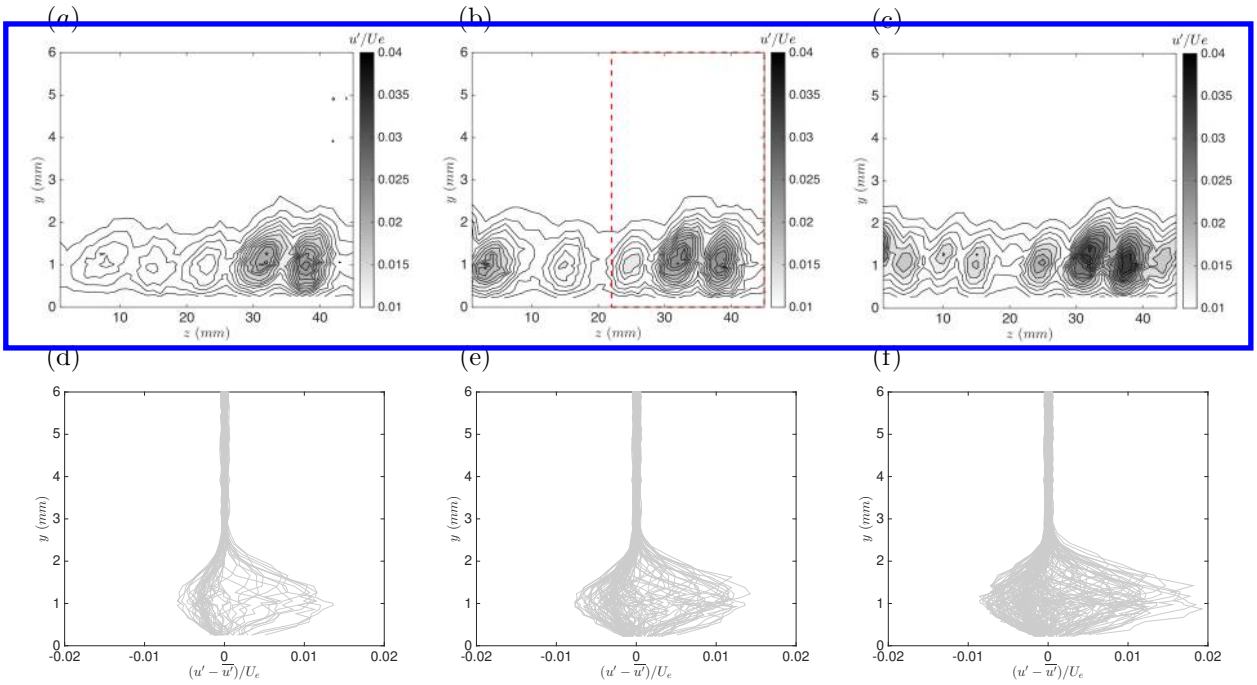

Figure 6. (top) Contour plots of non-dimensional fluctuating velocity profiles , u'/U_e, at $x/c = 35\%$ for (a) Natural, (b) L11_H24_1R and (c) L11_H24_2R cases. (bottom) Respective 2D spanwise variation, $(u' - \overline{u'})/U_e$. The dashed red box in (b) is discussed in figure 8.

pair of CFVs is embedded in each mean flow 'dune'. This is only true for this particular case L11_H24_2R, which was shown to contain a higher number of CFVs in the measurement regions, as highlighted when discussing figure 6(c).

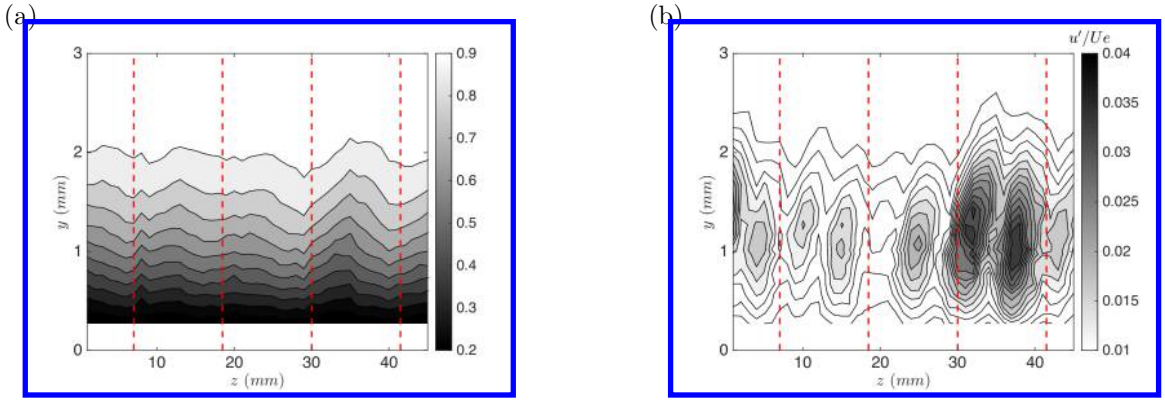

Figure 7. (a) **Contour plots of non-dimensional mean velocity profiles, U/U_e, and** (b) **contour plots of non-dimensional fluctuating velocity profiles, u'/U_e at $x/c = 35\%$ for L11_H12_2R case.**

To further explore the evolution of these CFVs along the test model, we dedicate our focus at the region bounded by the red box in figure 6(b). We focus on a region extending 23 mm in the spanwise direction, which corresponds to two critical wavelengths, λ. The result of this effort are shown in figure 8. In particular, we track the evolution of these two vortices in space from $x/c = 35\%$ to $x/c = 45\%$. Unfortunately, due to the natural inclination angle of the inviscid streamline (to which these vortices are reported to be closely related), this pair crosses and escapes our measurement domain downstream at $x/c = 45\%$. In particular, we do not have a full set of information on these CFVs in our $x/c = 45\%$ and $x/c = 50\%$ hot-wire scans (see figure 3). We only discuss the behaviour for the L11_H12_1R case, however, these findings have general

validity, as all our cases presented similar physics. It is also general in terms of the region of focus, as the flow should be reasonably two-dimensional once the DREs are employed. It can easily be seen that, while the vortices develop downstream, they gain strength and became bigger from a maximum height of about 2 mm at $x/c = 35\%$ up to a height of nearly 4 mm at $x/c = 45\%$. This zoomed-in domain also helps visualising the merging of these two vortices into one in (b). It is this merging mechanism driven by external flow entrainment that will eventually lead to the onset of turbulence. It is important to state, however, that at this stages, the flow is still laminar as these strengthen vortices are still bound by laminar flow pockets. More quantitatively, one can investigate the amplitude of these stationary crossflow instabilities. To do so, the contour plots of the velocity fields in figure 8 (a) to (c) can be collapsed in one dimensional form to visualise the mode shape of these travelling cross flow disturbances. This is commonly done in the literature (Hunt, 2011) by monitoring the quantity $rms[(u' - \overline{u'})/Ue]$. These results are shown in figure 8 (d) to (f) for $x/c = 35\%$, $x/c = 40\%$ and $x/c = 45\%$ respectively. As the flow develops downstream, these amplitude increase up to $\approx 450\%$ in between $x/c = 35\%$ and $x/c = 45\%$ (based on the maximum rms amplitudes).

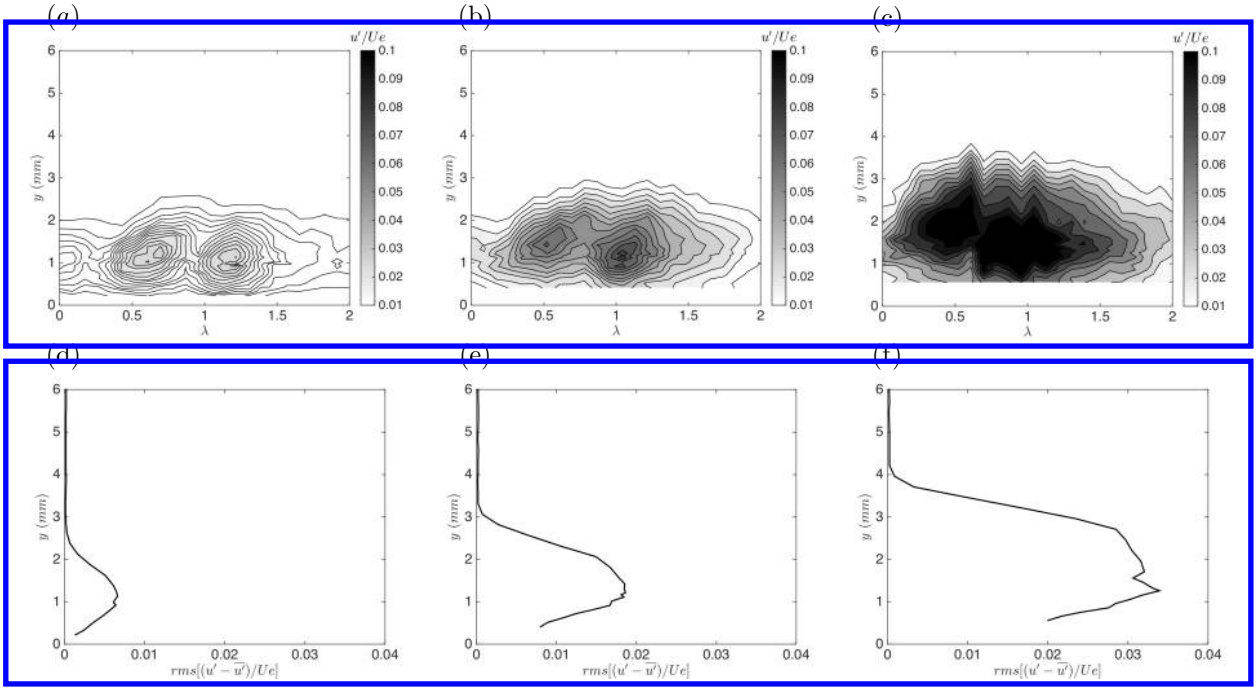

Figure 8. (top) Evolution non-dimensional fluctuating velocity profiles , u'/U_e, at (a) $x/c = 35\%$, (b) $x/c = 40\%$ and (c) $x/c = 45\%$ for L11_H12_1R case. (bottom) Respective travelling crossflow amplitude, $rms[(u' - \overline{u'})/Ue]$, at the same locations.

D. Amplitude and growth of stationary crossflow vortices

A similar analysis to that in figure 8 can be extended to the mean field in figure 5(a) to (c), so to investigate the evolution of the stationary CFVs along the chord line. The amplitude of the stationary crossflow disturbances are presented in figure 9. More specifically, for reasons to do purely with the page layout, only measurements at $x/c = 35\%$, $x/c = 40\%$, $x/c = 45\%$ and $x/c = 48\%$ are presented from (a) to (d) respectively. All cases investigated herein are included in these plots. As expected, starting at 35% chord (in figure 9(a)), both DREs cases are found to enhance the disturbance amplitude when compared to the Natural benchmark case. Although the difference with the Natural case are not appreciable in the figure 9(a), the effect of one row of DREs (i.e L11_H24_1R case) is to strengthen the CFVs amplitude by $\approx 17\%$, while the second row of roughness (i.e L11_H24_2R case) further increases it by $\approx 28\%$. This is perhaps not as high as previous studies have reported (Hunt, 2011). When one looks at the station $x/c = 40\%$ in figure 9(b), the L11_H24_2R case is found to have a greater effect on the amplitude of the stationary modes, which it is shown to be amplified by $\approx 13\%$ when compared with the L11_H24_1R case. Beyond 40% chord, it is

clear by looking at figure 9(*c*)&(*d*) that the mode shape is very different when compared with figure 9(*a*)&(*b*). A kink in the mode shapes appears in figure 9(*c*) in correspondence of $rms[(u-U)/Ue] = 0.035$. This is normally a feature present once the onset of nonlinear instability occurs (Dagenhart, 1992; Hunt and Saric, 2011). The profiles shown in figure 9(*d*) are shown to be highly distorted, presenting a 'second lobe' which is an indication of nonlinear distortion of the primary stationary crossflow mode (Eppink, 2014; Reibert, 1996). In figure 9(*c*), the case with a single row of DREs seems to take over in the forcing of the stationary modes, given the higher amplitude characterising the *rms* profiles in this case. The difference is in favour of the L11_H24_1R by 9%. Following the amplitude evolution downstream (in figure 9(*d*)), however, the L11_H24_2R case is found, once again, to provide higher forcing (by approximately 10%) in correspondence of $x/c = 50\%$. This inversion of the trend in dependence of the DREs geometry when providing high forcing for the stationary crossflow modes has to be further investigated.

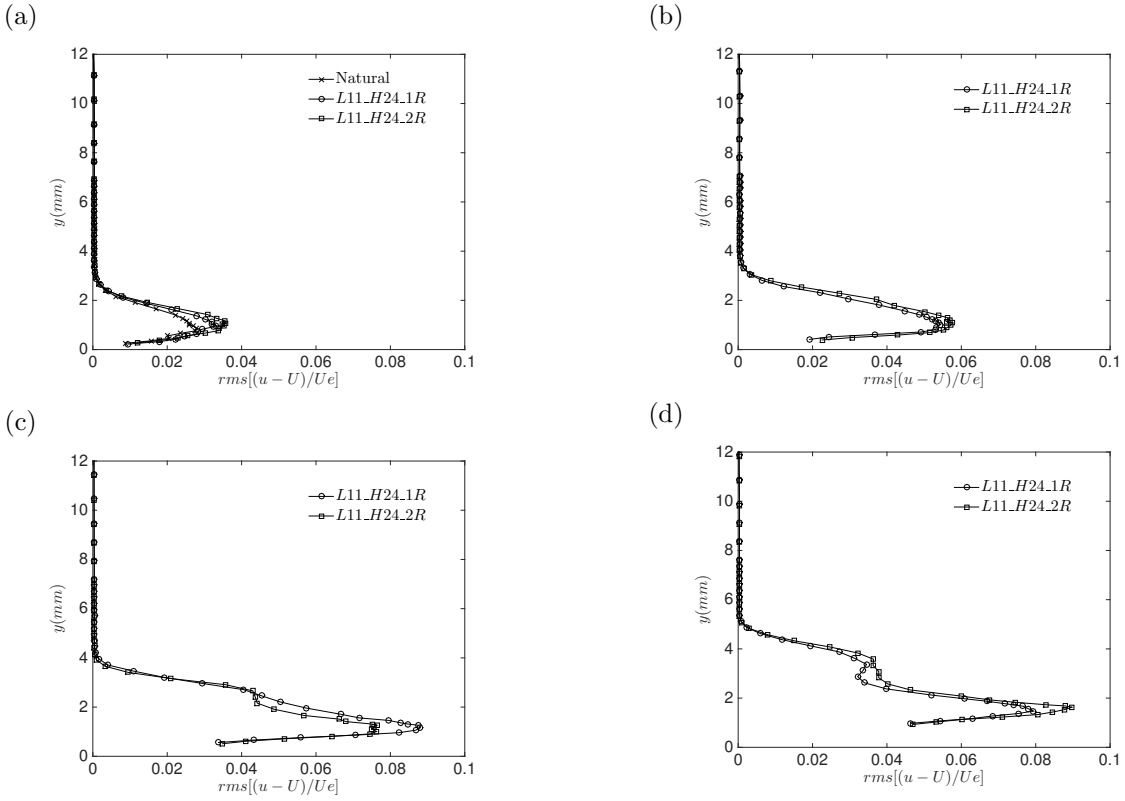

Figure 9. Amplitude of the CFVs, $rms[(u-U)/Ue]$, comparison at (*a*) $x/c = 35\%$, (*b*) $x/c = 40\%$, (*c*) $x/c = 45\%$ **and** (*d*) $x/c = 50\%$ **for Natural and roughness cases. Please note that amplitudes at** $x/c = 48\%$ **are here omitted.**

The mode shape reported in figure 9 can be also used to track the growth of the CFVs. Different methods for computing the amplitude of stationary CFVs can be employed, however, these were shown to be largely equivalent (Reibert, 1996). Only two ways are presented herein. Figure 10(*a*) shows results obtained by using the maximum value from the *rms* profile in figure 9, so that $A = max(rms[(u-U)/Ue])$. It is important to note that $A_{0.35}$ in this figure represent the amplitude at the first measurement location (i.e. $x/c = 35\%$); it is therefore highlighted that this curve cannot be translated into an N-factor curve, for obvious reasons. It is shown that, for all cases, the crossflow mode amplitudes growths up to 45% chord, after which it saturates to then reduce further downstream till a second growth stage (Malik et al., 1994) takes over again at 50% chord. The L11_H24_1R case seem to have the highest growth (up to $x/c = 45\%$), which seems somewhat counterintuitive. Results also show a recovery at $x/c = 50\%$ after which the L11_H24_2R case shows the fastest growth in mode amplitude. Another equivalent common method to quantify the amplitude of CFVs is to integrate the area under the curves over the entire stationary mode profile (in figure 9), so that $A = 1/\delta \int_0^\delta rms[(u-U)/Ue]\,\mathrm{d}y$. The result of this procedure is presented in 10(*b*). In agreement with Reibert (1996), these two methods are shown to be equivalent in terms of the trends in the growth of the disturbances. The absolute number are different but the behaviour of the two curve is identical. It is perhaps

worth commenting on the physical difference in between these two methods. While the maximum amplitude method focuses on the strength of the disturbances (given the maximum in the *rms* profile), the integration method is more intimately connected to the shape and size of these disturbances. Nevertheless, the size and strength of a vortex are closely related.

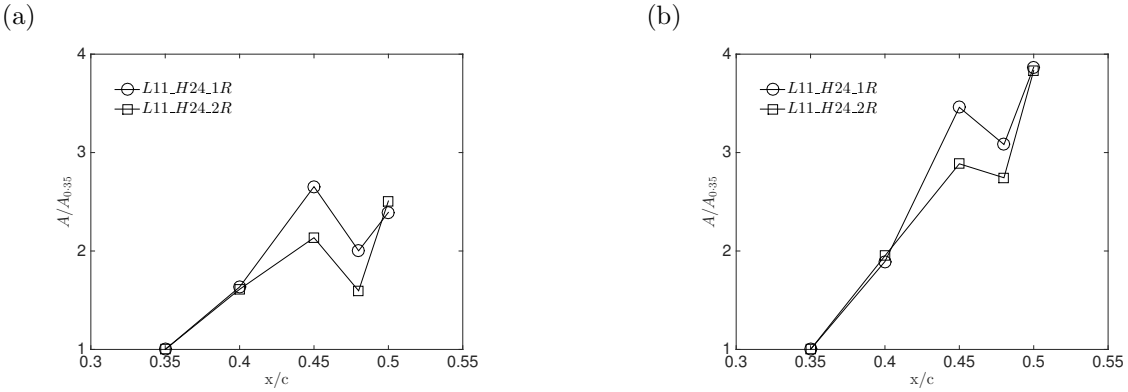

Figure 10. (*a*) **Growth of stationary CFVs based upon the maximum of the** *rms* **profile (**$A = max(rms[(u-U)/Ue])$**) and** (*b*) **growth of stationary CFVs based upon the integral area below the** *rms* **profile (**$A = 1/\delta \int_0^\delta rms[(u - U)/Ue]\,\mathrm{d}y$**).**

E. Spanwise spectral content

To explore the spatial content of the disturbances characterising the experiment described herein, a spatial power spectral density (PSD) analysis can be carried out. Before we discuss some results, it is important to point out some of the limitations of this analysis. Following Reibert (1996), for a spatial spectrum the wavelength resolution (i.e. inverse of the frequency in time signals) can be expressed as follows: $\Delta\lambda \approx \lambda^2/S$, where λ is the wavelength and S is the full length of measurement domain. In the current study, this results in a spatial resolution of approximately 2 mm. The minimum wavelength that can be resolved can also be estimated to be: $\lambda = 2\Delta S = 2S/(N-1) \approx 2$ mm. Given the size of the measurement domain, the spatial spectrum can therefore only be resolved with a meaningful resolution in the limited range $\lambda = 2 - 16$ mm. This is due to the fact that the hot-wire scans performed herewith were not optimised for these type of measurements. Obtaining a more resolved spatial spectrum, would require a much larger measurement domain (as increasing the sampling time would not affect the spatial resolution), which translated into a much longer run time. It was therefore deemed unfeasible. However, despite these limitations, the presented data is sufficient to draw some insightful conclusions. The power spectral density of the normalised signal velocity signals is presented in figure 11(*a*) to (*d*) for $35, 40, 45, 48\%$ chord locations. Please note that for formatting reasons amplitudes at $x/c = 50\%$ are here omitted. At the first measurement location (figure 11(*a*)), it is clear that all cases (and more so in presence of the roughness) show a clear PSD peak located at approximately 12 mm. It must, however be pointed out that the uncertainty at this wavelength is ± 3 mm. This is consistent with the imposed spanwise spacing of the DREs, for which $\lambda = 11.5$ mm (see § II). The natural case also shows some additional energy content below 4 mm, although barely visible here. This ties in well with the fact that this must be due to the inherent roughness on the plate surface. When DREs are superimposed on this roughness, however, they dominate the energy spectrum, dampening this contributions at $\lambda < 4$ mm. Following the evolution of the disturbances downstream the model in figure 11(*b*) high energy is still present at $\lambda = 12$ mm, and it is clear that the L11_H24_2R case provides the stronger primary mode forcing. The latter, together with the L11_H24_1R case also shows a secondary peak in the PSD in correspondence of $\lambda \approx 5$ $mm \approx \lambda/2$, which is consistent with previous finding in Reibert (1996). Forcing at λ also results in exciting modes at λ/n, where n is an integer number. This reduced spanwise spacing also ties in well with fluctuating fields shown in figure 6(*c*). A PSD peak is also visible for the natural case in correspondence of $\lambda \approx 2$ mm. When looking at the data beyond 45% chord (in figure 11(*c*)&(*d*)) it is noticeable that the energy peak tends to migrate toward $\lambda \approx 16$ mm. This is consistent with finding described in figure 8(*c*), for which two CFVs were found to merged into one at this chordwise location and this results in changing the critical wavelength of the dominant mode, hence increasing the characteristic

wavelength of the problem. However, it must be pointed out that some increase in the energy at shorter wavelength is also registered. These trends should be further confirmed.

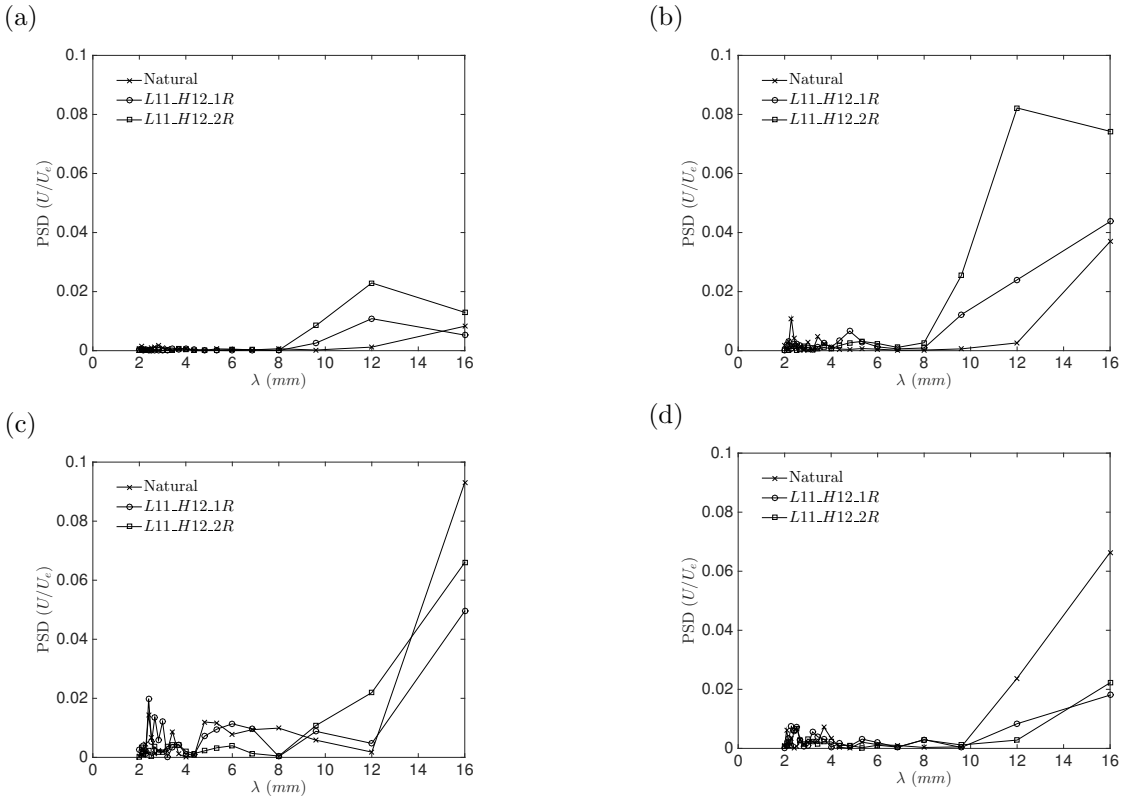

Figure 11. Power spectral density per unit wavelength at $x/c = 35, 40, 45, 48\%$ chord from (a) to (d). Please note that results for $x/c = 50\%$ are here omitted.

F. Transition location

Evaluating the transition onset is probably the most important requirement for laminar flow wing designers, as this features prescribes the aerodynamic loads. Given the analysis of the CFVs development and their growth carried out in the previous sections, it is important to relate the latter with the onset of turbulence. Figure 12 shows the detected transition location as a function of the chord Reynolds number, based on the procedure discussed in § II. It is found that, in the natural case, transition occurs at 63% chord, this is due to the low environmental disturbance characterising our wind tunnel. When one row of 24 μm height DREs are employed (i.e. L11_H24_1R case) the transition front moves forward to 59% chord. Finally, the effect of the second array of roughness (i.e. L11_H24_2R), further contributes to move the onset of turbulence to 57% chord. It must be pointed out that these are substantial changes give that, following our assessment (see § II), our criterion is affected by an uncertainty of $\pm 0.3\%$ chord. It must however be pointed out that some degree of scatter across the spanwise direction is inevitable given the classical 'saw tooth' transition patter in crossflow studies (Anscombe and Illingworth, 1956). These are interesting findings, especially in the light of the growth of the crossflow modes described in § D. Although the growth of the stationary crossflow mode was shown to be the fastest for the L11_H24_1R case (at least in its first stage), this does not simply translates into an anticipated transition onset. These findings need to be further investigated. This seems to suggest that, not only the growth of the disturbances but also, intuitively, the nature of forcing plays a role in defining the onset of turbulence, which is perhaps not surprising. In other words, this work suggests that an additional degree of freedom plays a role in modulating the crossflow modes. When employing DREs one needs to considered not only the height of the roughness elements (Hunt, 2011) and the spanwise spacing of the latter (Reibert, 1996), but also the pattern in use. We attempted to preliminary demonstrate that, by keeping the forcing at fixed wavenumber (as in between cases L11_H24_1R and L11_H24_2R), the physical distribution of the DREs onto the surface intimately affects the stability of 3D boundary layers.

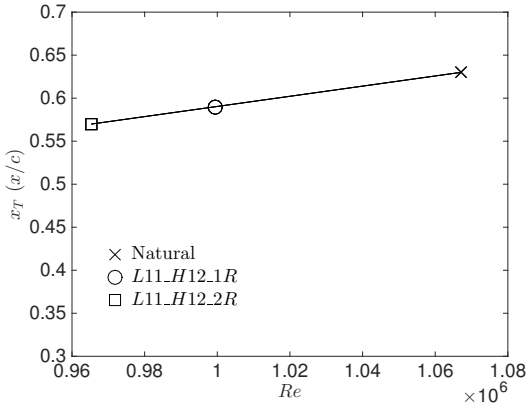

Figure 12. Transition location as a function of chord Reynolds number, Re.

IV. Conclusions and future work

Hot-wire experiments were conducted in a low-turbulence environment ($Tu < 0.006\%$) on the stability of 3D boundary layers. The effect of two different surface roughness distributions on crossflow vortices disturbances and their growth was evaluated. A comparison between mean and fluctuating velocity fields in the Natural case (here taken as a benchmark) and the different discrete roughness geometries were provided.

DREs were found to be an effective tool in modulating the instability of crossflow modes, although the effect of $24\mu m$ DREs was found to be somehow less effective than previously reported in the literature. These finding should be further investigated but our suspicion falls onto a combined effect of weaker favourable pressure gradient and lower level of environmental disturbances when compared to previous studies.

The L11_H24_1R case was found to be characterised by a faster growth of the disturbances in early stages, when compared to the L11_H24_2R case, however this trend was inverted into the second growth stage. This faster first stage growth did not simply translate into an earlier transition onset. The preliminary findings of this work suggest that together with the height of the DREs (Hunt, 2011) and their spanwise spacing (Reibert, 1996), their distribution across the surface (at fixed excited wavelengths) greatly affects the stability of 3D boundary layers. As expected, the case characterised by the rougher surface, leads to earlier transition.

This paper also reports evidences on tracking the development of a pair of CFVs along the chord of the model and capturing the merging of the pair, which is accompanied by a change in the characteristic wavelength of the problem in examination. This phenomenon was also captured via spatial power spectral density analysis.

Future work should include a more in depth analysis of the data and investigation on more complex roughness distributions. Some of the findings reported herein needs to be further investigated as they are in disagreement with some of the previous work on DREs. Furthermore, hints of the presence of travelling CFVs were found in wind tunnel data despite the very low-turbulence intensity characterising the facility. Further effort should be devoted to quantify the presence of the latter. Finally, despite the great attention dedicated to polish the surface of the model, this aspect could be improved to reduce the environmental contamination due to the natural roughness of the plate (which was found in the spatial spectral analysis) and some additional work can be put into improving the leading edge joint.

Acknowledgments

The authors are grateful to Innovative UK and Airbus for supporting this research under the Advanced Laminar Flow Enabling Technique (ALFET) Project. We also acknowledge the support from the NWTF for some of the tunnel instrumentations under the EPSRC Grant Ref. EP/L024888/1.

References

Anscombe, A. and Illingworth, L. N. (1956). Wind Tunnel Oservation of boundary-Layer Transition on a Wing at Various Angles of Sweepback. Technical report, Aeronautical research council.

Atkin, C. (2004). Performance trade-off studies for a retrofit Hybrid Laminar Flow Control system. *AIAA-2004-2215*, pages 1–11.

Bertolotti, F. P. (2000). Receptivity of three-dimensional boundary-layers to localized wall roughness and suction. *Physics of Fluids*, 12(7):1799.

Bippes, H. (1999). Basic experiments on transition in three-dimensional boundary layers dominated by crossflow instability. *Progress in Aerospace Sciences*, 35:363–412.

Bippes, H., Muller, B., and Wagner, M. (1991). Measurements and stability calculations of the disturbance growth in an unstable three-dimensional boundary layer. *Physics of Fluids*, 10:2371–2377.

Blasius, H. (1908). Grenzschichten in Flussigkeiten mit kleiner Reibung. *Z. Math. Phys.*, 56:1–37.

Bruun, H. H. (1995). *Hot-wire Anemometry Principles and Signal Analysis*. Oxford University Press.

Carpenter, A. L., Saric, W. S., and Reed, H. L. (2009). In-Flight Receptivity Experiments on a 30-Degree Swept- Wing using Micron-Sized Discrete Roughness Elements. In *47th AIAA Aerospace Sciences Meeting Including The New Horizons Forum and Aerospace Exposition AIAA 2009-590 5 - 8 January 2009, Orlando, Florida*, pages 1–32.

Carpenter, M. H., Carpenter, M. H., Cholemari, M. R., Cholemari, M. R., Craik, A. D. D., Craik, A. D. D., Chang, C.-L., Chang, C.-L., Li, F., and Li, F. (2010). Excitation of Crossflow Instabilities in a Swept Wing Boundary Layer. *48th AIAA Aerospace Sciences Meeting Including the New Horizons Forum and Aerospace Exposition Orlando, Florida*, pages AIAA 2010–378.

Choudhari, M. M. (1994). Roughness-Induced Generation of Crossflow Vortices in Three-Dimensional Boundary Layers. *Theoret. Comput. Fluid Dynamics*, 6:1–30.

Crawford, B. K., Duncan, G. T. J., Tufts, M. W., Saric, W. S., and Reed, H. L. (2015). Effect of local conditions on step-excrescence induced laminar-turbulent transition. In *50th 3AF International Conference Applied Aerodynamics Toulouse, France, 30-31 March, 1 April, 2015*, pages 1–10.

Crouch, J. D., Ng, L. L., Kachanov, Y. S., Borodulin, V. I., and Ivanov, A. V. (2015). Influence of surface roughness and free-stream turbulence on crossflow-instability transition. *Procedia IUTAM*, 14:295–302.

Dagenhart, J. R. (1992). *Crossflow stability and transition experiments in a swept-wing flow*. PhD thesis, Engineering Mechanics.

Deyhle, H. and Bippes, H. (1996). Disturbance growth in an unstable three-dimensional boundary layer and its dependence on environmental conditions. *Journal of Fluid Mechanics*, 316:73–113.

Eppink, J. (2014). *The interaction of crossflow instabilities and a backward facing step in swept boundary layer transition*. PhD thesis, Mechanical Engineering.

Eppink, J. and Wlezien, R. (2011). Data Analysis for the NASA/Boeing Hybrid Laminar Flow Contrl Crossflow Experiment. In *41st AIAA Fluid Dynamics Conferene and Exhibit 27 - 30 June 2011, Honolulu, Hawaii*, pages AIAA 2011–3879.

Gray, W. (1952). The effect of wing sweep on laminar flow. . Technical Report 256, RAE.

Hunt, L. E. (2011). *Boundary-Layer Receptivity to Three-Dimensional Roughness Arrays on a Swept-Wing*. PhD thesis, Texas A&M University. Aerospace Engineering Department.

Hunt, L. E. and Saric, W. S. (2011). Boundary-Layer Receptivity of Three-Dimensional Roughness Arrays on a Swept-Wing. In *41st AIAA Fluid Dynamics Conference and Exhibit 27 - 30 June 2011, Honolulu, Hawaii*, pages AIAA 2011–3881.

Kachanov, Y. S. (1994). Physical mechanisms of laminar-boundary-layer transition. *Annual Review of Fluid Mechanics*, 26:411–482.

Kachanov, Y. S. (2000). Three-dimensional receptivity of boundary layers. *European Journal of Mechanics - B/Fluids*, 19:723–744.

Ligrani, P. M. and Bradshaw, P. (1987). Spatial resolution and measurement of turbulence in the viscous sublayer using subminiature hot-wire probes. *Experiments in Fluids*, 5(6):407–417.

Malik, M. R., Li, F., and Chang, C.-L. (1994). Crossflow disturbances in three-dimensional boundary layers: nonlinear development, wave interaction and secondary instability. *Journal of Fluid Mechanics*, 268:1–36.

Mangalam, S. and Pfenninger, W. (1984). Wind-tunnel tests on a high performance low-Reynolds number airfoil. In *13th AIAA Aerodynamic Testing Conference, SanDiego, CA*, pages AIAA 1984–0628.

Morkovin, M. V. (1969). *On the Many Faces of Transition*. Viscous Drag Reduction. Springer.

Mughal, M. S. and Ashworth, R. M. (2013). Uncertainty Quantification Based Receptivity Modelling of Crossflow Instabilities Induced by Distributed Surface Roughness in Swept Wing Boundary Layers. In *AIAA 2013-3106. 43rd AIAA Fluid Dynamics Conference,24-27 June, San Diego, CA*, Reston, Virginia. American Institute of Aeronautics and Astronautics.

Radeztsky, R. H. (1994). *Growth and Development of Roughness-induced Stationary Crossflow Vortices*. Arizona State University.

Radeztsky, R. H. J., Reibert, M. S., and Saric, W. S. (1999). Effect of Isolated Micron-Sized Roughness on Transition in Swept-Wing Flows. *AIAA Journal*, 37(11):1370–1377.

Reed, H. L. and Saric, W. S. (1989). Stability of three- dimensional boundary layers. *Annual Review of Fluid Mechanics*, 21:235–284.

Reed, H. L. and Saric, W. S. (1996). Linear stability theory applied to boundary layers. *Annual Review of Fluid Mechanics*, 28:389–428.

Reibert, M. S. (1996). *Nonlinear stability saturation and transition in crossflow dominated boundary layers*. PhD thesis, Aerospace Engineering Department.

Reshotko, E. (1976). Boundary-Layer Stability and Transition. *Annual Review of Fluid Mechanics*, 8:311–349.

Saeed, T. I., Morrison, J. F., and Mughal, M. S. (2014). Roughness effects on swept-wing crossflow transition in moderate free-stream turbulence. In *29th Congress of International Council of the Aerospace Sciences*, pages 1–17.

Saric, W. S. (2008a). Experiments in 2-D Boundary Layers: Stability and Receptivity. Technical report, Aerospace Engineering Department Texas A&M University.

Saric, W. S. (2008b). Flight experiments on local and global effects of surface roughness on 2-d and 3-d boundary-layer stability and transition . Technical report, Aerospace Engineering Department Texas A&M University.

Saric, W. S. and Reed, H. L. (2003). Crossflow instabilities - Theory & technology. In *AIAA 2003-0771*, pages 1–9. AIAA 2003-0771.

Saric, W. S., Reed, H. L., and Kerchen, E. J. (2002). Boundary-layer receptivity to freestream disturbances. *Annual Review of Fluid Mechanics*, 34:291–319.

Saric, W. S., Reed, H. L., and White, E. B. (2003). Stability and transition of three-dimensional boundary layers. *Annual Review of Fluid Mechanics*, 35(1):413–440.

Shapiro, P. J. (1977). The influence of sound upon laminar boundary layer instability. Technical Report 83458-83560-1, Massachusetts Institude of Technology.

Tani, I. (1969). Boundary-layer transition. *Annual Review of Fluid Mechanics*, 1:169–196.

Tempelmann, D., Schrader, L. r.-U., Hanifi, A., BRandt, L., and Henningson, D. S. (2012). Swept wing boundary-layer receptivity to localized surface roughness. *Journal of Fluid Mechanics*, 711:516–544.

Tufts, M. W., Reed, H. L., and Saric, W. S. (2014). Design of an Infinite-Swept-Wing Glove for In-Flight Discrete-Roughness-Element Experiment. *Journal of Aircraft*, 51(5):1618–1631.

van Bokhorst, E., Placidi, M., and Atkin, C. (2015). Design of an experimental setup to investigate the development of the crossflow instability. In *Third International Academic Conference of Postgraduates, NUAA,Nanjing, P.R.China,18-20 November*, pages 1–7.

van Bokhorst, E., Placidi, M., and Atkin, C. J. (2016). The influence of the spatial frequency content of discrete roughness distributions on the development of the crossflow instability. In *AIAA Aviation 2016, 13-17 June, Washington, D.C.*

Wang, Y. X. and Gaster, M. (2005). Effect of surface steps on boundary layer transition. *Experiments in Fluids*, 39(4):679–686.

White, E. B. and Saric, W. S. (2005). Secondary instability of crossflow vortices. *Journal of Fluid Mechanics*, 525:275–308.